

# P-type $\delta$ -doping with Diborane on Si(001) for STM Based Dopant Device Fabrication

Tomáš Škřeň,\* Sigrun Köster, and Andreas Fuhrer<sup>†</sup>

*IBM Research – Zrich, Samerstrasse 4, 8803 Rschlikon, Switzerland*

Bastien Douhard and Claudia Fleischmann

*IMEC, Kapeldreef 75, 3001 Heverlee, Belgium*

## Abstract

Hydrogen resist lithography using the tip of a scanning tunneling microscope (STM) is employed for patterning p-type nanostructures in silicon. For this, the carrier density and mobility of boron  $\delta$ -layers, fabricated by gas-phase doping, are characterized with low-temperature transport experiments. Sheet resistivities as low as  $300 \Omega$  are found. Adsorption, incorporation and surface diffusion of the dopants are investigated by STM imaging and result in an upper bound of 2 nm for the lithographic resolution which is also corroborated by fabricating a 7.5 nm wide p-type nanowire and measuring its electrical properties. Finally, to demonstrate the feasibility of bipolar dopant device fabrication with this technique, we prepared a 100 nm wide pn junction and show that its electrical behavior is similar to that of an Esaki diode.

## I. INTRODUCTION

Definition of atomically sharp dopant profiles is a challenge in device fabrication as scaling of electronic devices approaches the few nanometer range<sup>1-4</sup>. Limits in achievable doping densities and unwanted diffusion of the dopants into the channel, impact both access resistance and variability of today's semiconductor devices. On the other hand, single dopants have become a resource as artificial atoms, embedded in near perfect crystalline semiconductors sometimes referred to semiconductor vacuum. They are used e.g. for qubits<sup>5</sup> or charge pumps<sup>6</sup>. Hydrogen resist lithography using an STM has achieved both atomically sharp dopant profiles<sup>7</sup> and deterministic patterning of single dopant devices<sup>8</sup>.

Hydrogen termination of the Si(001) surface with a mono hydride strongly suppresses the surface reactivity. Subsequent local desorption of the hydrogen using the tip of an STM creates local reaction sites (dangling bonds) where gas phase dopant precursors attach and can be incorporated into substitutional silicon surface sites. For phosphine this process is well established and low temperature incorporation is possible without significant diffusion of the dopants (for a review see Ref. <sup>9</sup>). However, degenerately doped p-type acceptor devices have not been explored so far with this technique. Patterning of acceptor structures at the nanoscale is crucial in terms of the implications for fabrication of p-type field effect transistors, but also to explore e.g. STM fabrication of bipolar planar dopant devices or to exploit electric field tunability of acceptor spin states for spin manipulation<sup>10</sup>.

In the present work, we investigate gas-phase  $\delta$ -doping with diborane ( $B_2H_6$ ) for p-type acceptor device fabrication with an STM, and find resistivities that compare well with those of phosphorus  $\delta$ -doped layers and donor devices<sup>9</sup>. While full activation of boron requires higher temperatures than for phosphorus, we show that patterning of acceptor devices with hydrogen resist lithography is possible, and blurring of the patterned device after annealing can be limited to a few nanometers. We employ the p-type doping technique to fabricate an acceptor nanowire and, in combination with n-type doping, a bipolar pn-junction.

## II. RESULTS AND DISCUSSION

In order to establish a method for p-type gas phase doping with diborane for STM-based dopant device fabrication several fundamental requirements need to be fulfilled. First, con-

ditions for the reaction of diborane with the Si surface need to be established such that the surface is saturated with the dopant precursor but avoiding unintentional surface passivation with hydrogen gas, present in the precursor as a carrier gas. Second, an important prerequisite for hydrogen resist lithography is the selective adsorption of diborane to areas of the Si:H surface which have been de-passivated by the STM tip. Finally, it is important to confirm that the boron  $\delta$ -layer can be encapsulated by overgrowth with a Si layer without segregation, preserving its atomic sharpness. The validity of these conditions is investigated in the first part of the paper.

In the second part we present electrical transport properties of boron doped  $\delta$ -layers and their dependence on diborane dose and activation temperature.

In the last part we detail the fabrication procedure and electrical measurements of two dopant devices which involve selectively diborane doped p-type areas. The first one is a 7.5 nm wide p-type nanowire and the second one is a 100 nm wide pn-junction which combines diborane p-type doping with previously established n-type doping based on phosphine.

### A. p-type $\delta$ -doping

In a first step, we use room temperature STM imaging to investigate the sticking and surface reaction of diborane on Si(001). Previous work found that saturation dosing of the Si(001) surface requires doses of up to 1000 L at room temperature<sup>11,12</sup>. However, heating of the silicon substrate was shown to improve sticking of the diborane molecule due to improved surface dissociation. We want to limit temperatures during dosing to below 450 °C such that patterns written into the hydrogen resist remain intact<sup>13</sup>. Furthermore, while molecular hydrogen (the carrier gas) does not stick to the silicon surface at room temperature, dissociative adsorption of H<sub>2</sub> on the silicon surface is known to increase with temperature<sup>14</sup>. This led us to select a sample temperature of 200 °C during diborane dosing which ensures that structures patterned using STM lithography stay intact and have acceptable doping densities.

Figure 1a shows a filled state STM image of a bare silicon surface after exposure to 3 L of diborane at 200 °C (see Methods for details about dose interpretation). The image spans two atomic silicon steps on which some residual silicon dimer rows can be identified. We observe three distinct levels in the topography of each terrace where the residual dimer rows

have an intermediate height. Furthermore, there are both darker depressions and brighter protrusions. The dark areas can be identified as the parts of the silicon surface that are hydrogen terminated. Here, both the carrier gas  $\text{H}_2$  and the diborane molecule  $\text{B}_2\text{H}_6$  are potential sources of hydrogen. Furthermore, it was previously suggested that some boron hydride fragments may appear similar to a hydrogenated silicon dimer<sup>15</sup>.

As with phosphine<sup>16</sup>, the maximum achievable boron density through gas phase doping is expected to be limited by unintentional surface passivation with hydrogen present in  $\text{B}_2\text{H}_6$ <sup>11</sup>. However, we also need to clarify the effect of the  $\text{H}_2$  carrier gas on this process<sup>14</sup>. The surface in Figure 1b was exposed to 230 L of pure molecular hydrogen at 220 °C. We find that about

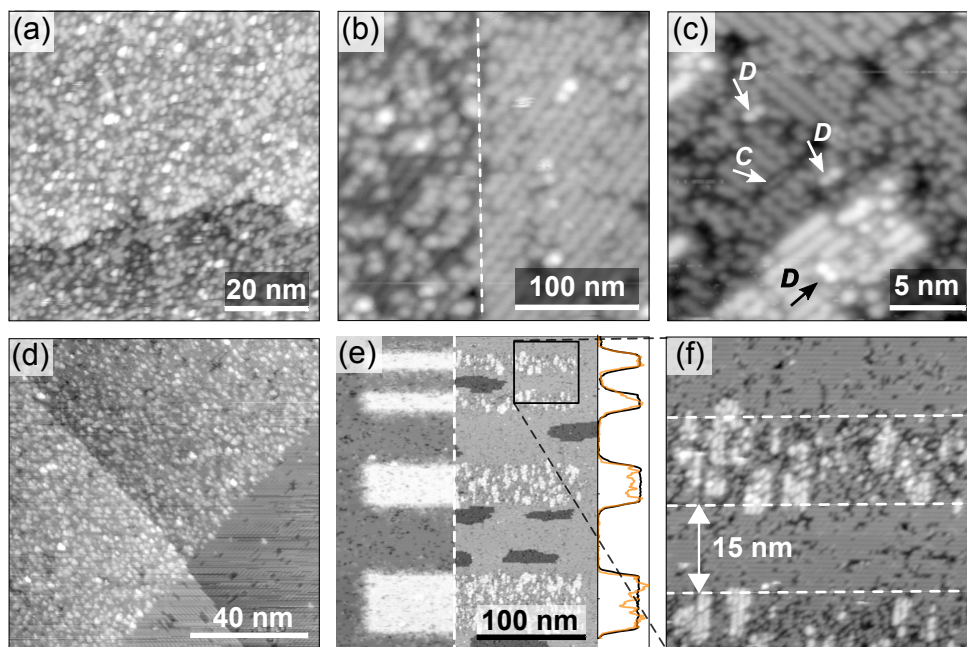


FIG. 1. STM investigation of adsorption and surface reactions of diborane with with the Si(001) surface. (a) Si(001) surface prepared by flash annealing in UHV and exposed to 3 L of diborane (30% in  $\text{H}_2$ ) at 200 °C. (b) Si surface exposed to 230 L of pure  $\text{H}_2$  under similar conditions as in (a). The right half was subsequently desorbed using the STM. (c) The surface shown in (a) after annealing at 510 °C for 5 min. *C* and *D* denote features related to boron in the silicon surface. (d) Edge of an STM-desorbed patch after exposure to 90 L of diborane at 180 °C. (e) Desorbed stripes after exposure to 90 L of diborane at 180 °C and a subsequent incorporation anneal for 1 min at 510 °C. To the right a scaled averaged line-cut of the stripes before (black) and after (brown) incorporation is shown. (f) Higher resolution image of the narrowest stripes in (e).

half of the surface is covered by hydrogen through surface dissociation, as shown in the left part of the STM image. On the right side of the image hydrogen was subsequently desorbed using the STM tip. This suggests that only a small fraction of the hydrogen in Figure 1a, with a more than 20 times smaller dose, originates from the H<sub>2</sub> carrier gas. Our choice of 200 °C as a dosing temperature therefore is a good trade-off between the surface reactivities of B<sub>2</sub>H<sub>6</sub> and H<sub>2</sub>. After dosing we further heat the sample to incorporate the boron into the silicon surface. Thermal decomposition studies indicate that only hydrogen desorbs into the gas-phase while boron remains on the surface and incorporates into substitutional sites at temperatures above 400 °C<sup>12</sup>.

Figure 1c shows an image of the surface in 1a after annealing to 510 °C for 5 min. Here, we can identify several features which have been attributed to boron atoms in the surface, namely a double dot protrusion marked *D* and an arrangement of indented atoms marked *C*. Both have been discussed before for samples annealed at similar temperatures<sup>11,15,17</sup>. While the *C* feature is not easy to identify, the *D* feature seems to be typical for substitutional boron on Si(001) replacing one of the two Si surface dimer atoms at low boron density<sup>17</sup>. In addition to this, there are still several depressions which we attribute to strain induced defects in the silicon surface. These STM images show that B<sub>2</sub>H<sub>6</sub> adsorbs on the silicon surface at 200 °C and boron is at least partially incorporated into the silicon crystal after further annealing. More precise quantification of the effect of the incorporation anneal is obtained from transport measurements on boron  $\delta$ -layers in the next section.

In the following we now establish selectivity of the hydrogen resist towards diborane dosing and investigate the persistence of the structures during the annealing process. For this, we pattern the hydrogen terminated Si surface using the STM tip and study the evolution of these structures after dosing and annealing. Figure 1d shows adsorption of the diborane on an STM patterned surface (upper left part has been desorbed). After dosing the surface with 90 L of diborane, the border of a patterned patch remains sharply defined on the nanometer scale. While a high coverage of bright protrusions is visible inside the patch, the mono-hydride surface outside (lower right corner) remains practically unaltered.

The STM defined pattern remains stable even after annealing at temperatures  $T_A$  high enough to desorb the hydrogen resist. Figure 1e shows a pattern of 4 STM defined patches dosed with 90 L of diborane at 180 °C after 1 min anneal to  $T_A = 510$  °C. Even though clear changes in surface morphology occur, the stripes are still well resolved. The dark

islands represent the next Si layer below the surface. They are visible everywhere on the sample surface and are most likely caused by etching during the removal of hydrogen. In the regions exposed to diborane we find bright agglomerates which show dimer row formation as can be seen in the zoom in Figure 1f. We believe this to be ejected silicon atoms that have exchanged place with incorporated boron and start to form islands due to diffusion. While it is difficult to clearly identify the boron, we assume that the incorporated boron atoms move no further than the ejected silicon on the surface. This means that even at  $T_A = 510^\circ\text{C}$ , the resolution of p-type dopant device patterning is expected to be significantly better than 2 nm. The two line-traces in 1e are horizontally averaged line cuts (arbitrarily scaled in z) of the four patches before and after annealing. The good overlap of the two traces further supports the high resolution of the pattern transfer.

$\delta$ -doping and subsequent encapsulation by Si overgrowth can be accompanied by another complication which has also been encountered in the case of phosphine  $\delta$ -doping. During the overgrowth, dopant segregation can lead to blurring of the  $\delta$ -doping profile and, ultimately, deterioration of the inplane resolution<sup>18</sup>. In the case of phosphorus doping, this problem has been addressed by using a so-called locking layer i.e. the first few monolayers of the Si encapsulation layer are grown at lower temperature to suppress segregation while the rest of the overgrowth is performed at an elevated temperature in order to preserve the crystalline quality of the capping layer and decrease the number of defects<sup>19</sup>.

In boron  $\delta$ -doped layers we find that segregation is less of a concern. Secondary ion mass spectroscopy (SIMS) measurements were performed on two samples: S1 (default preparation as shown in Fig. 2a ) and S2 (includes locking-layer as shown in Fig. 2b ).

SIMS traces for  $^{11}\text{B}$  (solid lines) and  $^{10}\text{B}$  (dashed lines) are shown in Figs. 2c (linear scale) and 2d (logarithmic scale) with the correct isotopic ratio and for both samples. The consistent behavior of the two isotopes for each sample is a confirmation that the SIMS data is not influenced by other atomic species.

For both samples the leading edge (left side) of the SIMS profile has a slightly smaller slope indicating that there is some boron segregation during overgrowth. This is stronger for the trace of sample S1 (blue trace) which exhibits a shoulder towards the surface. This means that the locking layer can indeed improve the sharpness of the boron  $\delta$ -doping profile, however, the measured characteristics are very similar for both samples and, compared to phosphorus doping, segregation of the dopants does not represent a substantial issue.

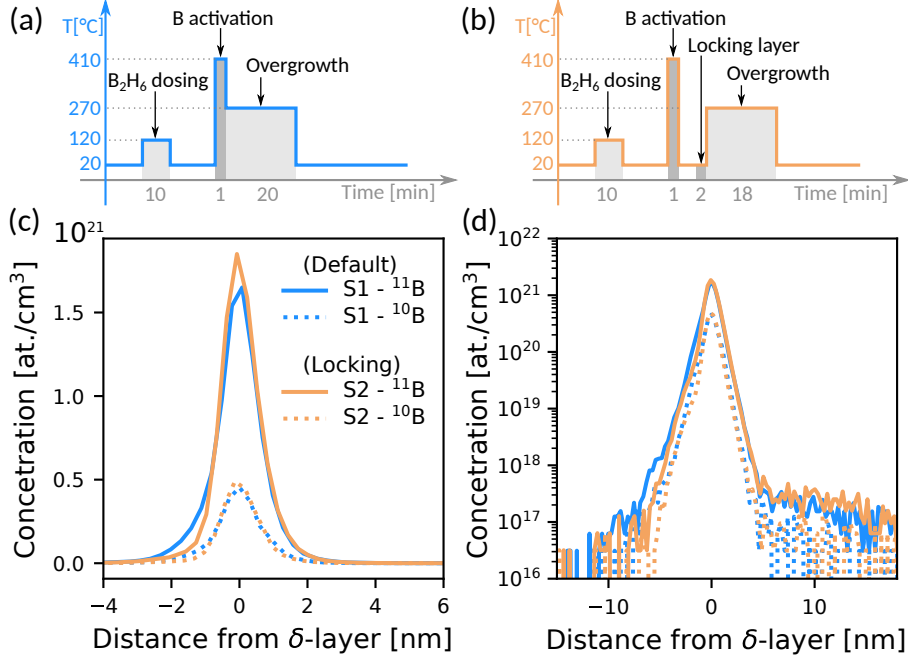


FIG. 2. Sample preparation and SIMS measurements of boron doped  $\delta$ -layers. (a) Preparation procedure of sample S1 (default): after dosing with diborane and a 1 min activation anneal at 410 °C the  $\delta$ -layer is immediately overgrown with 20 nm of intrinsic silicon at a temperature of 275 °C. (b) In sample S2 (locking-layer) the sample is first cooled to room temperature after the activation anneal. A 2 nm thick layer of Si is grown before raising the sample temperature to 275 °C and growing the rest of the Si layer. (c, d) SIMS concentration profiles of the two samples: S1 (blue) and S2 (brown). Solid lines are for  $^{11}\text{B}$  dashed lines for  $^{10}\text{B}$ .

Furthermore, a FWHM of 1.4 nm for the  $\delta$ -layer thickness is already close to the theoretical resolution limit of the SIMS technique and gives an upper limit of the real thickness. These SIMS measurements therefore show that dopant segregation is negligible when using boron as a dopant and the use of a locking layer is not necessary. This can be seen as a clear advantage over phosphorus since the required low temperature growth is usually associated with the formation of defects and lower overgrowth Si layer quality<sup>19</sup>.

## B. Transport measurements on p-type $\delta$ -layers

We use e-beam lithography to pattern Hall bars from the  $\delta$ -layer samples and anneal them at different temperatures  $T_A$  to study activation of the dopants. Figure 3a shows the

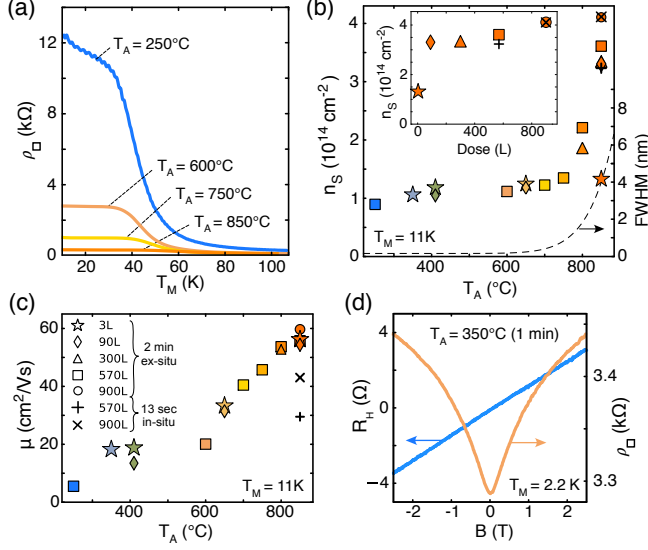


FIG. 3. (a) Resistivity of a 570 L  $\delta$ -layer sample as a function of measurement temperature  $T_M$  annealed ex-situ at  $T_A$  for 2 min. (b) Sheet density and (c) mobility as function of annealing temperature  $T_A$ . The inset in (b) shows the weak dependence of  $n_S$  on diborane dose at  $T_A = 850^\circ\text{C}$ . The legend for graphs (b) and (c) is given in (c). (d) Longitudinal  $\rho_{\square}$  and transverse  $R_H$  magnetoresistance of the 3L sample, annealed in-situ at  $T_A = 350^\circ\text{C}$  for 1 min.

resistivity per square  $\rho_{\square}$  as a function of measurement temperature  $T_M$  for a  $\delta$ -layer sample with a dose of 570 L annealed for 2 min in forming gas. For  $T_M > 35\text{ K}$ , substrate conductivity strongly influences the measured resistivity. Below this temperature the carriers in the low-doped substrate freeze out and measurements reflect the properties of the boron  $\delta$ -layers. In the following, only this lower temperature range is considered.  $\rho_{\square}$  clearly drops with increasing  $T_A$ , giving values as low as  $300\ \Omega/\square$  for anneals at  $850^\circ\text{C}$ . For  $T_A > 250^\circ\text{C}$  the resistivities of the  $\delta$ -layers show only a weak temperature dependence down to  $T_M = 0.1\text{ K}$  (not shown).

Figure 3b shows the sheet density  $n_S$  and Figure 3c the Hall mobility  $\mu$  of all the samples that were investigated. Without additional annealing we find a sheet density of  $10^{14}\text{cm}^{-2}$  for all samples and little changes up to  $T_A = 700^\circ\text{C}$ . From the bulk diffusivity of boron in silicon we estimate that the full width at half the maximum of the boron distribution starts to increase at  $T_A = 650^\circ\text{C}$ , as shown by the dashed line in Figure 3b (calculated for a 2 min anneal). We find that  $n_S$  increases in sync with this broadening of the boron distribution, reaching densities as high as  $4 \times 10^{14}\text{cm}^{-2}$ . This corresponds to the maximum density



expected from the surface reaction model put forward in Ref.<sup>11</sup> where  $\text{BH}_2$  and H terminate the broken  $\pi$ -bond of every surface Si dimer. The observed increase in active carrier density can be explained by two possible dopant (de)activation processes. First, the low temperature overgrowth may leave the dopant atoms in interstitial sites or generally create crystal defects at the growth interface that deactivate a fraction of the charge carriers. However, from previous experiments with phosphorus we do not expect this to be a significant concern. The second effect is dopant deactivation because of the proximity of the boron atoms. The broadening of the  $\delta$ -layer with increasing  $T_A$  leads to an increased spacing between dopants and a decrease in local density  $\rho_{3D}$ . For  $T_A = 750^\circ\text{C}$ , we estimate  $\rho_{3D} = 2 \times 10^{21} \text{cm}^{-3}$ . At this density theoretical considerations indicate that, depending on the microscopic arrangement, only about one third of the dopants are expected to be active<sup>20</sup>. This is in agreement with our observations. However, it would mean that only about one boron atom per cubic Si unit cell can be active, which is significantly less than what was estimated in samples created by other techniques<sup>21,22</sup>. Furthermore, it is not entirely clear why the dosing procedure we use always gives roughly the same initial density of  $10^{14} \text{cm}^{-2}$  irrespective of the actual exposure dose. Contrary to what one may have expected from previous STM studies<sup>11,12</sup>, we find no dependence on exposure dose for doses of 90 L or higher after annealing at  $850^\circ\text{C}$  (see inset in Figure 3b). The only sample which shows a sheet density that is clearly limited by the initial exposure dose is the 3 L sample (filled stars).

The mobility  $\mu$  is expected to be determined by ionised impurity scattering. For this situation it was discussed in Ref.<sup>22</sup> that  $\mu$  should depend only on the active carrier concentration, similar to findings with n-type dopants. However, we find that  $\mu$  increases in a more gradual fashion with  $T_A$  than the sheet density. This may indicate that disorder at the regrowth interface or clustering of the dopants within the  $\delta$ -layer also play a role for  $\mu$ . The fact that the 3 L sample shows a slightly higher mobility for low  $T_A$  supports this, since we expect the initial dopant separation to be larger in this situation. Moreover, this sample has a factor of three lower density than the other samples at  $T_A = 850^\circ\text{C}$ , while the mobility is again similar. In an attempt to fully activate the dopants while limiting the broadening of the  $\delta$ -layer, we also performed short 13 sec in-situ anneals using direct current heating of two highly dosed samples at  $T_A = 850^\circ\text{C}$ . We anneal the samples after overgrowth with 2 nm of silicon and before standard encapsulation with silicon. This is indicated by the two cross symbols in Figures 3b, c. We find that we can fully activate the dopants even though the

FWHM of the dopant distribution is estimated to be only 1.4 nm. The mobility is, however, clearly reduced which is consistent with the expected higher value of  $\rho_{3D}$ . Note that it is difficult to control the short duration and temperature of the anneal in-situ and we therefore expect more variability of the measured parameters for these samples.

This series of experiments shows that for full activation of the boron acceptors annealing temperatures  $T_A > 800^\circ\text{C}$  are necessary. Nevertheless, it also demonstrates that boron can be incorporated at temperatures below  $450^\circ\text{C}$ , which is both compatible with hydrogen resist lithography and gives resistivity values  $\rho_{\square}$  similar to those in n-type devices<sup>9</sup>. To support this, Figure 3d shows the longitudinal magnetoresistance of the 3L boron sample after annealing at  $350^\circ\text{C}$  for 1 min, i.e. using identical conditions as for phosphorus donor device fabrication. In contrast to phosphorus  $\delta$ -layers a positive magnetoresistance is expected for boron<sup>23</sup> and we find a roughly four times higher  $\rho_{\square}$ , which is in equal part due to a lower  $\mu$  and  $n_S$ .

### C. p-type nanowire and gap

In the following we combine boron p-type  $\delta$ -doping with STM lithography and create a p-type device with three terminals containing a nanowire on one side and a gap on the other. The temperatures and times used for the different steps of device fabrication are the same as in 2a. The detailed description of the device fabrication process and ebeam contacting procedure can be found in<sup>24</sup>.

The device outline with the patterned dimensions is shown in Figure 4c along with an STM image of the desorbed pattern before dosing with diborane in Figure 4d. Figures 4a, b show the electrical measurements of the Gap and Nanowire segment at a temperature of 2.5 K. The nanowire shows Ohmic conductivity around 0 V bias while the gap only shows current after reaching a threshold voltage of about 20 mV, as expected for a tunnel junction. This threshold of 20 mV is slightly lower than the voltage observed for a tunnel junction with a similar geometry but for a phosphorus doped device<sup>24</sup>. By measuring the resistance of the nanowire section we can estimate the sheet resistivity of the boron doped layer to be  $5\text{ k}\Omega \cdot \square^{-1}$ .

These results show that the p-type nanowire device behaves in a similar way as expected from a corresponding n-type dopant device. The sheet resistivity of the p-type layer is

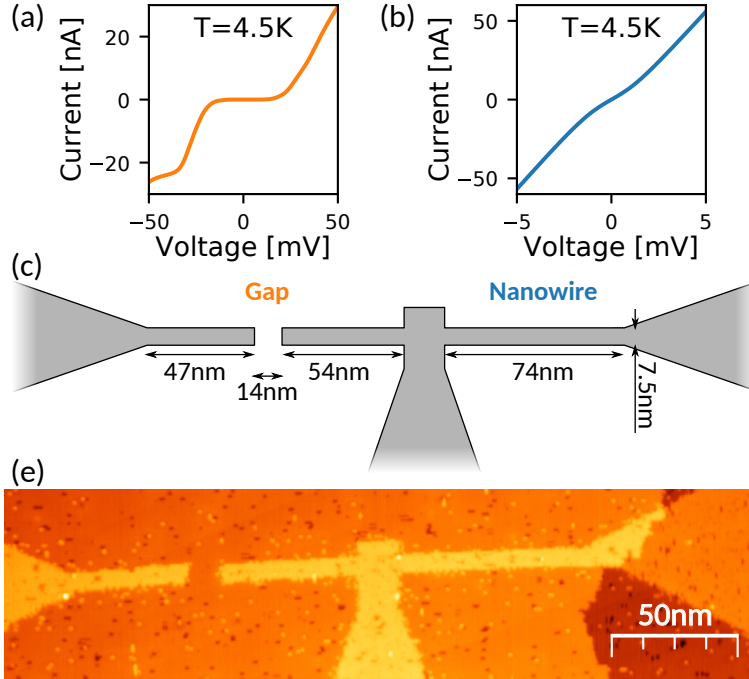


FIG. 4. Electrical measurements of the STM defined boron doped dopant device. (a, b) Current-voltage characteristics of the gap and nanowire section of the device. (c) Schematic drawing of the device with dimensions and (d) the STM image of the device area after the desorption of the H layer with the STM.

slightly higher due to limited dopant activation at the temperatures available for this process. Moreover, the sheet resistivity as well as contact resistance has been more variable for p-type devices than for corresponding phosphorus doped n-type devices. The critical step is probably the activation anneal which would have to be very tightly controlled in order to achieve precisely reproducible resistivities.

#### D. pn-junction

After developing the method for p-type  $\delta$ -doping and constructing a p-type nanoscale device, an obvious next step is to combine p- and n-type doping in a single sample to fabricate a pn-device. The most simple bipolar device is a two terminal pn-junction.

The procedure for bipolar device fabrication is a two step process which is outlined in Figure 5a. In a first step, we use the STM to define the areas for p-type doping, dose the sample with diborane and perform the activation anneal. The reason we start with

p-type doping is that the thermal budget is slightly higher in this case and, as such, we prevent unnecessary exposure of the n-type doped areas to these higher temperatures. The temperature we use for the boron activation ( $410^{\circ}\text{C}$ ) already leads to a partial desorption of the H passivation layer from the Si surface and renewal of the H layer is required by exposing the sample to atomic hydrogen at a temperature of  $323^{\circ}\text{C}$ . Subsequently, the sample is transferred back to the STM stage and hydrogen resist patterning for the n-type doping step is performed. The critical step here is alignment of the n-type pattern to the previously doped p-type area. This is achieved by careful placement of the device within the optical localization marker pattern using an optical microscope. We then use the STM to scan a  $8 \times 8$  micron area and identify the patch with ejected silicon from the first doping step. Figure 5b shows an STM image of the central part of the pn-junction after the desorption of the area for n-type doping in the lower part of the pattern. The boron doped area can be seen in the upper part of the image. After STM desorption, the sample is dosed with phosphine, the activation anneal is performed and, finally, the sample is overgrown with a 20 nm layer of intrinsic Si. Scanning electron (SEM) image of the finished pn-device is presented in Figure 5c. The n- (p-type) areas show dark (bright) contrast in SEM imaging with the in-lens detector respectively. This behavior is often observed when imaging doped semiconductors and stems from the energy sensitivity of this detector. Subsequently, the device was contacted using e-beam-defined metallic contacts and the sample was placed in a package and wire bonded.

Current-voltage characteristic of the pn-junction measured at a temperature of 1.7 K are shown in Figures 5d, e. The pn-junction is expected to exhibit asymmetric behavior with higher conductivity in the forward direction (positive voltage). This behavior can be seen for voltages higher than  $\sim 0.6$  V (region 4 in Figure 5d). Further, for the reverse-bias direction (negative voltage) we can see a gradual increase of the current (region 1). This is related to the high doping density on both sides of the pn junction - the depletion region around the pn junction is narrow and allows tunneling of the charge carriers. The conduction is also dominated by the tunneling current in the forward direction in region 2. In region 3, the current again drops which is caused by misalignment of the bands in p- and n-doped regions. This region of negative differential resistance is a characteristic feature for highly doped pn junctions (Esaki diode).

Fabrication of bipolar devices is not substantially more demanding than fabrication of

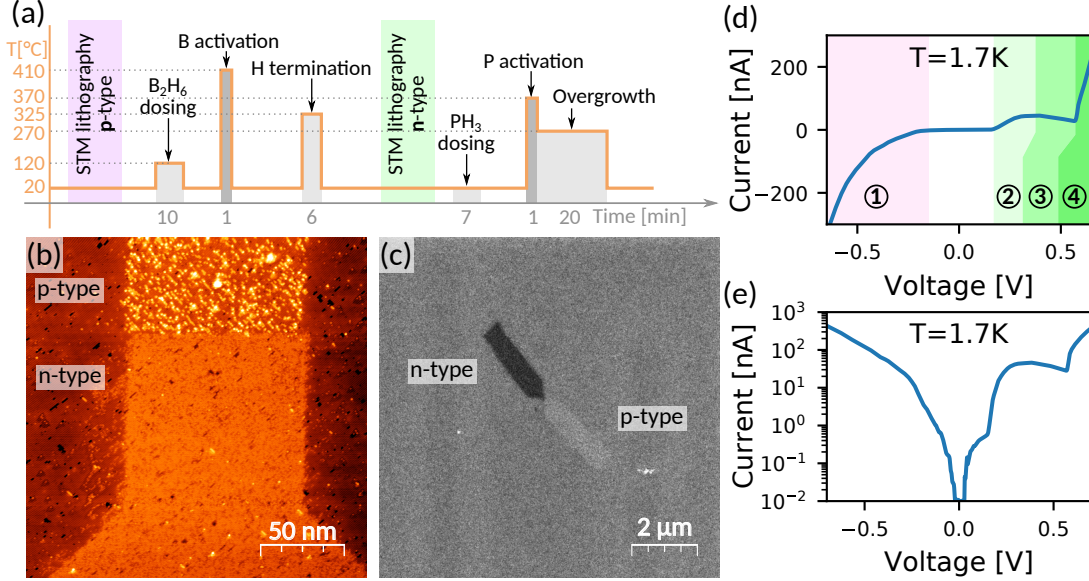


FIG. 5. Fabrication of a bipolar dopant device with STM lithography. (a) Preparation procedure, (b) STM image of the central part of the pn junction right after desorption of the area for phosphorus doping (lower part). In the upper section, boron doped and incorporated area is visible. (c) Ex-situ SEM image of the pn-device from (c). Linear (d) and semilog plot of the current-voltage characteristics of the pn junction.

an n- or p-type dopant device. The only additional step is the alignment of the STM tip to the previously doped region and this can be solved by proper choice of device position with respect to the optical localization markers. However, similarly to the remark about p-type devices in the previous section, there is larger variability in the sheet resistivities and contact resistances. For a number of pn-devices we even encountered issues with non-functional contacts, mostly to the p-type part of the device. We believe that these problems can be solved by better control of the boron activation step, however, these issues will require more detailed investigation before the technique can be adapted as routine method for bipolar dopant device fabrication.

### III. CONCLUSIONS

In conclusion, we have shown that hydrogen resist lithography can be used for STM-patterning of p-type nanostructures with a resolution better than 2 nm. Even though full activation of the dopants can only be reached at  $T_A = 850^\circ\text{C}$ , we demonstrate that boron

$\delta$ -layers with resistivities below  $3.3 \text{ k}\Omega$  can be fabricated using dosing and incorporation temperatures that are compatible with hydrogen resist lithography. To demonstrate the feasibility of this approach we fabricated a  $7.5 \text{ nm}$  wide p-type dopant nanowire which shows ohmic conductivity and resistivity of about  $5 \text{ k}\Omega\text{cm}^{-1}$ . By combining the p-type doping with established n-type doping we also prepared the first bipolar dopant device - a  $100 \text{ nm}$  wide pn-junction which behaves similar to an Esaki diode. These results open the way for fabrication of a large variety of more complex p-type and bipolar nanoscale dopant devices.

#### IV. METHODS

Samples are fabricated from  $2.7 \times 9 \text{ mm}$ , n-type Si(001) wafer pieces with a resistivity of  $0.1\text{-}1.0 \text{ }\Omega\text{cm}$ . For sample preparation and hydrogen termination we follow the procedure outlined in Ref.<sup>25</sup>.

For desorption of hydrogen with the STM tip we typically used a tunneling current setpoint of  $3 \text{ nA}$  and sample bias of  $+4.1 \text{ V}$  (for high resolution patterning of nanoscale parts) up to  $6.5 \text{ V}$  (for fast low resolution desorption of large areas).

Dopant pre-cursors are introduced through a leak valve directly into the STM chamber containing an Omicron VT STM/AFM system. For diborane dosing we use 30% diborane in molecular hydrogen ( $\text{H}_2$ ). The sample is positioned directly in the gas flux while maintaining the pressure in the chamber constant. The doses given refer to total gas exposure as calculated from chamber pressure multiplied by exposure time. This means that effective diborane doses are about a factor of three lower than what we state.

Silicon overgrowth is performed by sublimation from an intrinsic silicon filament with a typical rate of  $0.4 \text{ nm/min}$  while keeping the sample at  $270 \text{ }^\circ\text{C}$ . After this, further processing occurs ex-situ using standard lithography techniques. For contacting the p-type devices we used Pt contacts, since the Fermi level in Pt is closer to that of degenerately doped p-type Si leading to a lower Schottky barrier. In the case of bipolar devices, we used Al contacts.

The SIMS profiles (Cameca SC Ultra) have been acquired using a  $250 \text{ eV } \text{O}_2^+$  primary beam with an incidence angle of  $46^\circ$  to the sample normal (calculated based on the potentials).

The boron concentration was quantified by measuring a boron reference sample with a known boron concentration and by applying the RSF method point-by-point relative to the

Si matrix signal. The total crater depth of the reference sample was measured by stylus profilometry allowing to determine the current-normalized sputter rate value. This value was then applied point-by-point to all profiles relative to their primary current curves to account for sputter rate variations with the primary beam current.

The authors gratefully acknowledge financial support from EU-FET grants SiAM 610637, PAMS 610446 and from the Swiss NCCR QSIT.

---

\* t.skereen@gmail.com

† afu@zurich.ibm.com

- <sup>1</sup> D. J. Frank, R. H. Dennard, E. Nowak, P. M. Solomon, Y. Taur, and H.-S. P. Wong, Proceedings of the IEEE **89**, 259 (2001).
- <sup>2</sup> J. C. Ho, R. Yerushalmi, Z. A. Jacobson, Z. Fan, R. L. Alley, and A. Javey, Nature Materials **7**, 62 (2008).
- <sup>3</sup> B. Colombeau, B. Guo, H.-J. Gossman, F. Khaja, N. Pradhan, K. V. Waite, A. adn Rao, C. Thomidis, K.-H. Shim, T. Henry, and N. Variam, Phys. Stat. Sol. (a) **211**, 101 (2014).
- <sup>4</sup> R. Duffy, M. Shayesteh, K. Thomas, E. Pelucchi, R. Yu, A. Gangnaik, Y. M. Georiev, P. carolan, N. Petkov, B. Long, et al., J. Mat. Chem. C **2**, 9248 (2014).
- <sup>5</sup> J. T. Muhonen, J. P. Debollain, A. Laucht, F. E. Hudson, T. Sekiguchi, K. M. Itoh, D. N. Jamison, J. C. McCallum, A. S. Dzurak, and A. Morello, Nature Nanotech. **9**, 986 (2014).
- <sup>6</sup> B. Roche, R.-P. Riwar, B. Voisin, E. Dupont-Ferrier, R. Wacquez, M. Vinet, M. Sanquer, J. Splettstoesser, and X. Jehl, Nature Communications **4**, 1581 (2013).
- <sup>7</sup> S. R. Schofield, N. J. Curson, M. Y. Simmons, F. J. Rueß, T. Hallam, L. Oberbeck, and R. G. Clark, Phys. Rev. Lett. **91**, 136104 (2003).
- <sup>8</sup> M. Fuechsle, J. A. Miwa, S. Mahapatra, H. Ryu, S. Lee, O. Warschkow, L. C. L. Hollenberg, G. Klimeck, and M. Y. Simmons, Nature Nanotech. **7**, 242 (2012).
- <sup>9</sup> M. Simmons, F. Ruess, K. Goh, T. Hallam, S. Schofield, L. Oberbeck, N. Curson, A. Hamilton, M. Butcher, R. Clark, et al., Molecular Simulation **31**, 505 (2005).
- <sup>10</sup> J. van der Heijden, J. Salfi, J. A. Mol, J. Verduijn, G. C. Tettamanzi, A. R. Hamilton, N. Collaert, and S. Rogge, Nano Letters **14**, 1492 (2015).
- <sup>11</sup> Y. Wang, J. Shan, and R. J. Hamers, J. Vac. Sci. Techn. B **14**, 1038 (1996).

- <sup>12</sup> M. L. Yu, D. J. Vitkavage, and B. S. Meyerson, *J. Appl. Phys.* **59**, 4032 (1986).
- <sup>13</sup> K. Oura, J. Yamane, K. Umezawa, M. Naitoh, F. Shoji, and T. Hanawa, *Phys. Rev. B* **41**, 1200 (1990).
- <sup>14</sup> M. Dürr, Z. Hu, A. Biedermann, U. Höfer, and T. F. Heinz, *Phys. Rev. Lett.* **88**, 046104 (2002).
- <sup>15</sup> Y. Wang and R. J. Hamers, *J. Vac. Sci. Technol. A* **13**, 1431 (1995).
- <sup>16</sup> H. F. Wilson, O. Warschkow, N. A. Marks, N. J. Curson, S. R. Schofield, T. C. G. Reusch, M. W. Radny, P. V. Smith, D. R. McKenzie, and M. Y. Simmons, *Phys. Rev. B* **74**, 195310 (2006).
- <sup>17</sup> Z. Liu, Z. Zhang, and X. Zhu, *Phys. Rev. B* **77**, 035322 (2008).
- <sup>18</sup> K. E. J. Goh, L. Oberbeck, M. Y. Simmons, A. R. Hamilton, and R. G. Clark, *Applied Physics Letters* **85**, 4953 (2004), ISSN 00036951.
- <sup>19</sup> J. G. Keizer, S. Koelling, P. M. Koenraad, and M. Y. Simmons, *ACS Nano* **9**, 12537 (2015), ISSN 1936086X.
- <sup>20</sup> X. Luo, S. B. Zhang, and S.-H. Wei, *Phys. Rev. Lett.* **90**, 026103 (2003).
- <sup>21</sup> E. Bustarret, C. Marcenat, P. Achatz, J. Kacmarcik, F. Lévy, A. Huxley, L. Ortéga, E. Bourgeois, X. Blase, D. Débarre, et al., *Nature* **444**, 465 (2006).
- <sup>22</sup> B. E. Weir, L. C. Feldman, D. Monroe, , H.-J. Grossmann, R. L. Headrick, and T. R. Hart, *Appl. Phys. Lett.* **65**, 737 (1994).
- <sup>23</sup> P. Dai, P. Zhang, and M. P. Sarachik, *Phys. Rev. B* **45**, 3984 (1992).
- <sup>24</sup> N. Pascher, S. Hennel, S. Mueller, and A. Fuhrer, *New Journal of Physics* **18**, 083001 (2016).
- <sup>25</sup> A. Fuhrer, M. Fuchsle, T. C. G. Reusch, B. Weber, and M. Y. Simmons, *Nano Letters* **9**, 707 (2009).